Journal of Colloid and Interface Science 640 (2023) 100–109

Contents lists available at ScienceDirect

Journal of Colloid and Interface Science

journal homepage: www.elsevier.com/locate/jcis

Probing the coverage of nanoparticles by biomimetic membranes through nanoplasmonics

Jacopo Cardellini [a,b], Andrea Ridolfi [a,b,c,d], Melissa Donati [a], Valentina Giampietro [a], Mirko Severi [a], Marco Brucale [b,c], Francesco Valle [b,c], Paolo Bergese [b,e,f], Costanza Montis [a,b], Lucrezia Caselli [a,b,g,*], Debora Berti [a,b,*]

[a] Department of Chemistry "Ugo Schiff", University of Florence, Florence, Italy
[b] CSGI, Consorzio Sistemi a Grande Interfase, University of Florence, Sesto Fiorentino, Italy
[c] Istituto per lo Studio dei Materiali Nanostrutturati, Consiglio Nazionale delle Ricerche, 40129 Bologna, Italy
[d] Department of Physics and Astronomy and LaserLaB Amsterdam, Vrije Universiteit Amsterdam, Amsterdam, The Netherlands[1]
[e] Department of Molecular and Translational Medicine, University of Brescia, Brescia, Italy
[f] Consorzio Interuniversitario Nazionale per la Scienza e la Tecnologia dei Materiali, Florence, Italy
[g] Department of Physical Chemistry 1, University of Lund, SE-22100 Lund, Sweden[1]

GRAPHICAL ABSTRACT

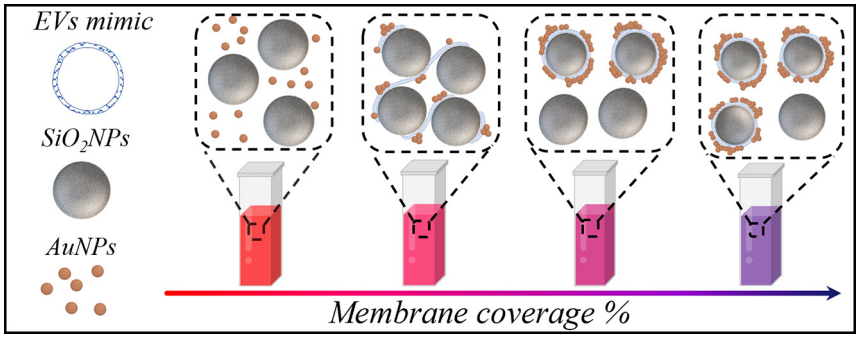

ARTICLE INFO

Article history:
Received 17 December 2022
Revised 29 January 2023
Accepted 13 February 2023
Available online 23 February 2023

Keywords:
Membrane-coated nanoparticles
Gold nanoparticles
Nanoplasmonics
Biomimetic nanoparticles
Silica nanoparticles

ABSTRACT

Although promising for biomedicine, the clinical translation of inorganic nanoparticles (NPs) is limited by low biocompatibility and stability in biological fluids. A common strategy to circumvent this drawback consists in disguising the active inorganic core with a lipid bilayer coating, reminiscent of the structure of the cell membrane to redefine the chemical and biological identity of NPs. While recent reports introduced membrane-coating procedures for NPs, a robust and accessible method to quantify the integrity of the bilayer coverage is not yet available. To fill this gap, we prepared SiO_2 nanoparticles (SiO_2NPs) with different membrane coverage degrees and monitored their interaction with AuNPs by combining microscopic, scattering, and optical techniques. The membrane-coating on SiO_2NPs induces spontaneous clustering of AuNPs, whose extent depends on the coating integrity. Remarkably, we discovered a linear correlation between the membrane coverage and a spectral descriptor for the AuNPs' plasmonic resonance, spanning a wide range of coating yields. These results provide a fast and cost-effective assay to

Abbreviations: SiO_2NPs, silica nanoparticles; AuNPs, gold nanoparticles; M-SiO_2NPs, membrane coated silica nanoparticles; EVs, Extracellular Vesicles.

* Corresponding authors.
E-mail addresses: lucrezia.caselli@fkem1.lu.se (L. Caselli), debora.berti@unifi.it (D. Berti), debora.berti@unifi.it (D. Berti).
[1] Current affiliation.

https://doi.org/10.1016/j.jcis.2023.02.073

Nano-bio interface
Extracellular vesicles
Nanomedicine

monitor the compatibilization of NPs with biological environments, essential for bench tests and scale-up. In addition, we introduce a robust and scalable method to prepare SiO_2NPs/AuNPs hybrids through spontaneous self-assembly, with a high-fidelity structural control mediated by a lipid bilayer.

1. Introduction

Over the last decades, numerous efforts have been devoted to the exploitation of the unique properties of inorganic nanoparticles (NPs) for biomedical applications. Despite a large number of NPs developed for biomedical purposes and reports illustrating their in-vitro potential, the route for effective clinical translation is still minimal due to multiple issues [1–5], including poor colloidal stability and limited circulation time in biological fluids, cytotoxic effects, poor targeting ability and uncontrolled accumulation in specific tissues, which eventually leads to low efficacy and unwanted side effects [6]. In a simplistic view, these drawbacks could be considered to be related to a general issue, i.e. the inherent exogenous, synthetic nature of inorganic NPs, and their size, which – being close to that of biomolecules and biological assemblies – can lead to unpredictable behavior when inserted into a biological environment. Coating NPs with a lipid membrane of either synthetic or natural origin is one of the most promising strategies to circumvent this issue, which led to a new class of nanomaterials, i.e., membrane-camouflaged biomimetic NPs. While retaining the physicochemical properties of the core (inorganic) material, the lipid shell of these systems provides biomimetic surface functions, such as immune escape ability and modulation, specific molecular recognition and targeting, enhanced cell adhesion, reduced toxicity, and long circulation time [7–12]. Among the possible sources for membrane camouflaging, synthetic lipid bilayers, whose composition can be conveniently tailored to resemble that of biological membranes, are commonly employed as bioinspired coatings to improve the biocompatibility and pharmacokinetics of NPs [13,14], as well as to enhance their colloidal stability [15]. Lipid bilayers can be easily functionalized to introduce targeting properties [16,17], steering the carriers towards specific sites, protecting them from the biological environment, and preventing the uncontrolled leakage of drugs [14]. More sophisticated coatings [18,19], employing natural cell membranes (e.g., of red [20-24] and white [25-27] blood cells, cancer cells [28-30], stem cells [31], platelets [32,33], and bacterial walls [34-36]), are currently the focus of intensive research, which has already led to the development of hybrid NPs with superior properties for drug delivery [37-39], in vitro imaging [20,40,41], diagnosis and treatment of cancer [42-44], bacterial infections [45,46] and other diseases [47], anticancer vaccination [10] and detection of viral pathogens [48]. In the palette of natural camouflages, the biomembrane of Extracellular Vesicles' (EVs') represents one of the latest -and more promising- frontiers [49]. EVs are biogenic vesicles naturally secreted by cells, containing lipids, proteins, nucleotides, and metabolites in the inner pool [50]. As compared to other natural membrane coatings, EVs provide unmet targeting abilities, which are connected to their role in cell–cell chemical communication as nano-shuttles for proteins, lipids, and RNA [51–53]. Provided by its endogenous origin, the EV membrane also offers near non-immunogenicity, resistance to macrophage uptake [52,54], and the ability to cross the blood–brain barrier [56,57], as well as enhanced endocytosis efficiency [58]. Coating NPs with the EVs membrane has recently proved as a powerful tool to achieve immune evasion-mediated targeting [59] and selective accumulation at the tumor site [59,60], e.g., through receptor-mediated endocytosis [61].

Despite the consistent growth of the library of available membrane-coated NPs, achieving complete membrane coverage and developing efficient and reliable methods to quantify its integrity remain significant hurdles. An incomplete membrane coating drastically decreases the colloidal stability of NPs [62–64], and may promote cargo leakage in drug-delivery systems [65]. Moreover, the integrity of the membrane coating modulates the efficiency of macrophage clearance [66] and affects the internalization mechanism of biomimetic NPs [67], as well as their biomedical functions [68–70].

So far, the characterization of the coating integrity has primarily relied on microscopy techniques (e.g., Electron, Confocal Laser Scanning, and Atomic Force microscopies) [71–73], Dynamic Light Scattering (DLS) [71], and Zeta Potential measurements [74–76]. However, microscopy techniques do not provide ensemble-averaged characterization and generally require specialized equipment and ad-hoc sample preparation. On the other side, scattering-based methods and other traditional approaches (e.g., colloidal stability test in phosphate-buffered saline or fetal bovine serum [67], and sodium dodecyl sulfate–polyacrylamide gel electrophoresis [74,77]) fail in providing a quantitative estimate of the coating extent. More sophisticated techniques, such as mass spectrometry (MS) or liquid chromatography-tandem MS [78–80], only give a rough estimation of the coating degree, i.e., heavily affected by strong assumptions on the morphology and structure of the coating itself.

Here, we report a new colorimetric and spectrophotometric method for quantitatively assessing the membrane coating extent based on the plasmonic properties of citrate-coated gold nanoparticles (AuNPs). AuNPs spontaneously interact with free-standing lipid bilayers, leading to membrane adhesion [81] and AuNPs clustering [82–88]. Recently, we have shown how the spontaneous clustering of AuNPs on synthetic and natural lipid vesicles (such as EVs) can be exploited to gain information on the characteristics of the vesicles themselves, such as their concentration [89], stiffness [90,91], and the presence of protein contaminants [92]. Overall, AuNPs plasmonic properties are emerging as convenient, highly sensitive, and robust probes for lipid interfaces. Given these unique properties, we here test the ability of AuNPs to probe and possibly quantify the membrane coating degree on the surface of inorganic NPs. To this purpose, we prepare biomimetic NPs with an inorganic silica core and a synthetic membrane shell, whose composition mimics the typical one of EVs. Through a combination of structural and spectrophotometric techniques, we investigate the interaction of such membrane-coated SiO_2NPs (M-SiO_2NPs) with AuNPs, as a function of the membrane coating integrity. Finally, we leverage these findings to estimate the extent of the lipid coverage of M-SiO_2NPs, through a simple and fast colorimetric assay.

2. Materials and methods

2.1. Materials

Tetrachloroauric (III) acid (≥99.9%) was provided by Sigma-Aldrich (St. Louis, MO). 1,2-Dioleoyl-*sn-glycero*-3-phosphocholine (DOPC) (≥99.0%), *N*-palmitoyl-D-*erythro*-sphingosylphosphorylcholine (sphingomyelin) (≥98.0%), and cholesterol (≥99.0%) were

provided by Avanti Polar Lipids. Sucrose, sodium chloride (NaCl) (≥99.5%), sodium citrate ($Na_3C_6H_5O_7$) (≥99.9%), and calcium chloride ($CaCl_2$) (≥99.999%) were provided by Sigma Aldrich. All chemicals were used as received. Milli-Q-grade water was used in all preparations. Silica Nanoparticles were provided by HiQ-Nano (Arnesano, Lecce, Italy) and are stable in an aqueous buffer and are characterized by a hydrophilic surface with terminal Si-OH functional groups.

2.2. Preparation of SiO_2NPs

The commercial batch was thoroughly homogenized by vortexing, followed by 30 min bath sonication before use. Subsequently, it was diluted in milliQ water to obtain a final SiO_2 concentration of 1.6 mg/mL right before mixing with liposomes.

2.3. Preparation of liposomes

To prepare the EVs-mimicking liposomes, the proper amount of DOPC, Sphingomyelin, and cholesterol was dissolved in chloroform (0.87/0.37/1 mol%/mol%), and a lipid film was obtained by evaporating the solvent under a stream of nitrogen and overnight vacuum drying. The film was then swollen and suspended in a warm (40 °C) water solution of sucrose (650 mM), sodium chloride (150 mM), and sodium citrate (10 mM) by vigorous vortex mixing to obtain a final lipid concentration of 7 mg/ml. The resultant multilamellar vesicles (MVL) in water were subjected to 10 freeze−thaw cycles and extruded 10 times through two stacked polycarbonate membranes with a 100 nm pore size at room temperature to obtain unilamellar vesicles (ULV) with a narrow and reproducible size distribution. The filtration was performed with the Extruder (Lipex Biomembranes, Vancouver, Canada) through Nucleopore membranes.

2.4. Preparation of membrane-coated silica nanoparticles (M-SiO_2NPs)

To prepare fully coated SiO_2-NPs, 1 mL of a dispersion of uncoated SiO_2-NPs in ultrapure water (1.6 mg/mL) was mixed with 1 mL of liposomes dispersion (7 mg/mL) at high stoichiometric excess of liposomes (approximately 1/50 SiO_2-NPs/liposomes number ratio), formed in an aqueous environment with high osmolality (650 mM sucrose, 10 mM Sodium Citrate, 150 mM NaCl, 10 mM $CaCl_2$). The formation of the lipid coating on SiO_2NPs starts with the adhesion of the vesicles on the SiO_2NPs surface due to Van der Waals interactions; this is followed by membrane rupture driven by the transmembrane gradient of osmotic pressure between the inner aqueous pool and the dispersing medium (SiO_2NPs were initially dispersed in ultrapure water). The excess of intact liposomes was then removed through centrifugation (6000 rpm × 30 min each), after which the supernatant was discarded, and the precipitate (containing M-SiO_2NPs) collected and redispersed in ultrapure water. This last step was repeated 6 times to fully remove the excess of intact vesicles. To account for possible material loss during the centrifugation cycles, the final concentration of M-SiO_2NPs was quantified by ICP-AES (see Section S2.3).

To prepare M-SiO_2-NPs with different degrees of coverage we employed the same protocol varying the initial SiO_2NPs/vesicle ratio. Specifically, 1 mL SiO_2-NPs in ultrapure water (1.6 mg/mL) was mixed with 1 mL of liposomes properly diluted to obtain SiO_2-NPs/vesicle ratios of approximately 1/15, 1/10, 1/5, 1/3, and 1/1. The intact liposomes were removed through centrifugation (6000 rpm × 30 min each), and the precipitate was collected and redispersed in 1 mL of ultrapure water.

2.5. Synthesis of AuNPs

Anionic gold nanospheres (AuNPs) of 12 nm in size were synthesized according to the Turkevich−Frens method [93,94]. Briefly, 20 mL of a 1 mm HAuCl4 aqueous solution was brought to the boiling temperature under constant and vigorous magnetic stirring. 2 mL of a 1% citric acid solution were then added to the mixture. The solution was further boiled for 10 min until it acquired a deep red color. The nanoparticle solution was then slowly cooled to room temperature.

2.6. Cryo-EM

3 μL of each sample at a SiO_2NPs concentration of 1.15 nM were applied on glow-discharged Quantifoil Cu 300 R2/2 grids. The samples were plunge-frozen in liquid ethane using an FEI Vitrobot Mark IV (Thermo Fisher Scientific) instrument. The excess liquid was removed by blotting for 1 s (blot force of 1) using filter papers under 100% humidity and at 10 °C. Cryo-EM data were collected at the Florence Center for Electron Nanoscopy (FloCEN), University of Florence (Italy), on a Glacios (Thermo Fisher Scientific) instrument at 200 kV equipped with a Falcon III detector operated in the counting mode. Images were acquired using EPU software with a physical pixel size of 2.5 Å and a total electron dose of ∼50 e−/Å2 per micrograph.

2.7. Atomic force microscopy (AFM)

NPs were deposited on top of poly-L-lysine (PLL) coated glass coverslips. All reagents were purchased from Sigma-Aldrich Inc (https://www.sigmaaldrich.com) unless otherwise stated. Menzel Gläser coverslips were cleaned in Piranha solution for 2 h and washed in a sonicator bath (Elmasonic Elma S30H) for 30′ in acetone, followed by 30′ in isopropanol and 30′ in ultrapure water (Millipore Simplicity UV). Before each experiment, glass coverslips were treated with air plasma (Pelco Easiglow) and immersed into a 0.01 mg/mL PLL solution in Borate buffer (pH 8.33) at room temperature for 30 min. After being thoroughly rinsed with ultrapure water and dried with nitrogen, the coverslips were ready to be used for the AFM experiments. A 10 μL droplet of the SiO_2NPs dispersion was deposited on top of the coverslips and left equilibrating for 15 min before being inserted into the AFM fluid cell. The concentrations of SiO_2NP dispersions were adjusted via trial and error to avoid the formation of NP-clusters, which would ultimately prevent the quantitative determination of their morphology. AFM experiments were performed in PeakForce mode at room temperature on a Bruker Multimode 8 equipped with Nanoscope V electronics, a sealed fluid cell, a type JV piezoelectric scanner, and Bruker SNL10-A probes (with nominal tip radius 2–12 nm and spring constant 0.35 N/m), calibrated according to the thermal noise method [95]. A 50 mM $MgCl_2$, 100 mM KCl solution was used as imaging buffer in order to reduce the electrical double layer (EDL) interaction region between the AFM tip and the NPs [96]. NP height was used to obtain the respective size distributions; given that NPs are spherical rigid objects, their height coincides with the NP diameter and, being unaffected by tip convolution effects, represents a reliable parameter for size estimation.

2.8. Dynamic light scattering (DLS) and ζ-Potential

DLS measurements at θ = 90° and the ζ-potential determination were performed using a Brookhaven Instrument 90 Plus (Brookhaven, Holtsville, NY). Each measurement was an average of 10 repetitions of 1 min each, and measurements were repeated 10 times. The autocorrelation functions (ACFs) were analyzed through cumulant fitting stopped at the second order for samples charac-

terized by a single monodisperse population, allowing an estimate of the hydrodynamic diameter of particles and the polydispersity index. ζ -potentials were obtained from the electrophoretic mobility u according to the Helmholtz − Smoluchowski equation $\zeta = (\frac{\eta}{\varepsilon}) \times \mu$ (1), where η is the viscosity of the medium and ε is the dielectric permittivity of the dispersing medium. The ζ-potential values are reported as averages from 10 measurements.

2.9. Inductively coupled plasma – atomic emission spectrometry (ICP-AES)

The determination of Si and P content in the samples was performed in triplicate by using a Varian 720-ES Inductively Coupled Plasma Atomic Emission Spectrometer (ICP-AES). An accurately measured amount of each sample was diluted to a final volume of 5 mL with 1% suprapure HNO_3 obtained by sub-boiling distillation. Each sample was thus spiked with 100 μL of Ge 50 mg/L standard solution used as the internal standard. Calibration standards were prepared by gravimetric serial dilution from a commercial stock standard solution of Si and P at 1000 mg L^{-1}. The analytic wavelengths used for Si and P determination were 251.611 and 213.618 nm, respectively, whereas for Ge we used the line at 209.426 nm. The operating conditions were optimized to obtain the maximum signal intensity, and between each sample, a rinse solution constituted of 2% v/v HNO_3 was used to avoid memory effects.

2.10. UV–vis spectroscopy

UV−vis spectra were recorded with a Cary 3500 UV−vis spectrophotometer. 50 μL of either naked SiO_2NPs or M-M-SiO_2NPs (at a SiO_2 concentration of 1.15 nM with different degrees of coverage were mixed with 300 μL of 6.13 nM AuNPs and incubated for 10 min at room temperature in PMMA UV–vis micro cuvettes (maximum volume 1.5 mL). Then, 700 μL of MilliQ water were added to the samples, and after 10 min, the spectra were simultaneously recorded with a multiple sample holder in the spectral range 350–800 nm.

2.11. Small angle X-ray scattering

M-M-SiO_2NPs/AuNPs hybrids were characterized at the SAXS beamline of the synchrotron radiation source Elettra (Trieste, Italy), which was operated at 2 GeV and a 300 mA ring current. The experiments were carried out with λ = 1.5 Å, and the SAXS signal was detected with a Pilatus 3 1 M detector in the q-range from 0.009 to 0.7 $Å^{-1}$. The SAXS curves were recorded in a glass capillary.

3. Results and discussion

3.1. Formation of biomimetic membrane-coated SiO_2NPs (M-SiO_2NPs)

As model inorganic particles, we selected commercial anionic SiO_2NPs, given their well-known surface chemistry and the wide range of applications in biomedical research [97,98]. To form the lipid coating, we used DOPC (1,2-dioleoyl-*sn-glycero*-3-phospho choline)/Sphingomyelin/Cholesterol (0.87/0.38/1.00 mol%) vesicles, characterized by an average hydrodynamic diameter of 110 nm (PDI 0.150) and a ζ -potential of −15.2 ± 1.3 mV (see section S2 of SI). Composition-wise, these synthetic membranes do not account for the complexity observed in biomembranes, which typically feature an impressive number of different proteins, lipids and (in the case of EVs) nucleic acids. Nevertheless, the above lipid composition has been specifically selected to retain the hallmark feature of EVs membranes, shared among EVs of different sources and biological functions, i.e., the typical enrichment in sphingomyelin and cholesterol, as compared to parental cells [99]. Thus, in spite being highly simplified, these synthetic systems can still represent effective models for the prototypical features of the lipid membrane of EVs. The lipid coating of SiO_2NPs was obtained through a slight modification of a well-established protocol [100] (described in the Materials and Methods section). Briefly, this method relies upon mixing SiO_2NPs in ultrapure water with a high stoichiometric excess of liposomes (≥1/50 SiO_2NPs/liposomes number ratio), formed in an aqueous medium with high osmolality. The adhesion of vesicles on the SiO_2NPs surface, driven by Van der Waals attractive forces, is quickly followed by membrane rupture, triggered by the transmembrane gradient of osmotic pressure between the inner aqueous pool of vesicles and the dispersing medium. M-M-SiO_2NPs were imaged through Cryogenic electron microscopy (Cryo-EM), with Fig. 1a and 1b displaying representative Cryo-EM images at different magnifications. While only very few intact vesicles appear to sit onto the SiO_2 surface (see Fig. 1a, top part, and section S2.1 for additional images), most of SiO_2NPs are either totally or partially (Fig. 1b red arrows) surrounded by a nanometric layer, closely following the particle morphology, with an electron density that is intermediate between the ones of SiO_2 and the surrounding medium. This layer can be reasonably identified as the bilayer, originally constituting the lipid membrane of vesicles. To gain additional information on the thickness of the surrounding layer, the samples were also imaged by liquid-Atomic Force Microscopy (AFM). Representative AFM images of SiO_2NPs and M-M-SiO_2NPs are displayed in Fig. S2.2, while Fig. 1c reports the size distributions obtained for the two samples; the average diameter for the SiO_2-NPs is 125 ± 10 nm, while the one of M-SiO_2NPs is 140 ± 15 nm. The 15 nm difference between the two average diameters is compatible with the presence of a lipid bilayer entirely covering most of the particles of the M-SiO_2NP sample. In addition, we characterized the lipid coating at an ensemble-averaged level, performing DLS and ζ -Potential measurements (Fig. 1d). The DLS autocorrelation functions for bare and M-SiO_2NPs (Fig. 1d) were analyzed through a cumulant fitting stopped at the second order [101]. The inset in Fig. 1d summarizes the main results. The hydrodynamic diameter of uncoated SiO_2NPs, inferred from the corresponding autocorrelation function, is 165 nm (PDI 0.067). It is worth highlighting that the hydrodynamic size of SiO_2NPs is remarkably larger (∼40 nm) than the primary particle diameter determined by AFM, which is in line with previous reports [102]. In contrast, the autocorrelation function of M-M-SiO_2NPs decays at longer times, consistent with an increase of hydrodynamic diameter up to 210 nm (PDI 0.1), which is compatible with an extensive formation of a lipid bilayer on the SiO_2NPs. Moreover, the characteristic ζ -Potential increases from −40 ± 1 mV (for SiO_2NPs) to –22 ± 1 mV (for M-SiO_2NPs), which is very close to the one of liposomes (-15 ± 1 mV), further confirmation of the effective lipid coverage of the SiO_2NPs' surface. Lastly, we quantified the extent of the SiO_2 surface covered by the lipid bilayer employing Inductively Coupled Plasma-Atomic Emission Spectrometry (ICP-AES). This technique allows for exact quantification of the Si and P atoms in the final M-SiO_2NPs samples, from which the ratio between the covered and bare SiO_2 surfaces can be inferred through simple geometrical models (see section S5.1 in SI). It is worth stressing that these models heavily rely on specific assumptions about the packing of lipid molecules within the membrane formed on SiO_2 (see section 2.3 of SI); consequently, the technique can only provide a rough estimation of the degree of coverage of the SiO_2NPs surface. Through this approach, a coverage % of 88 ± 8 was estimated for the sample reported in Fig. 1.

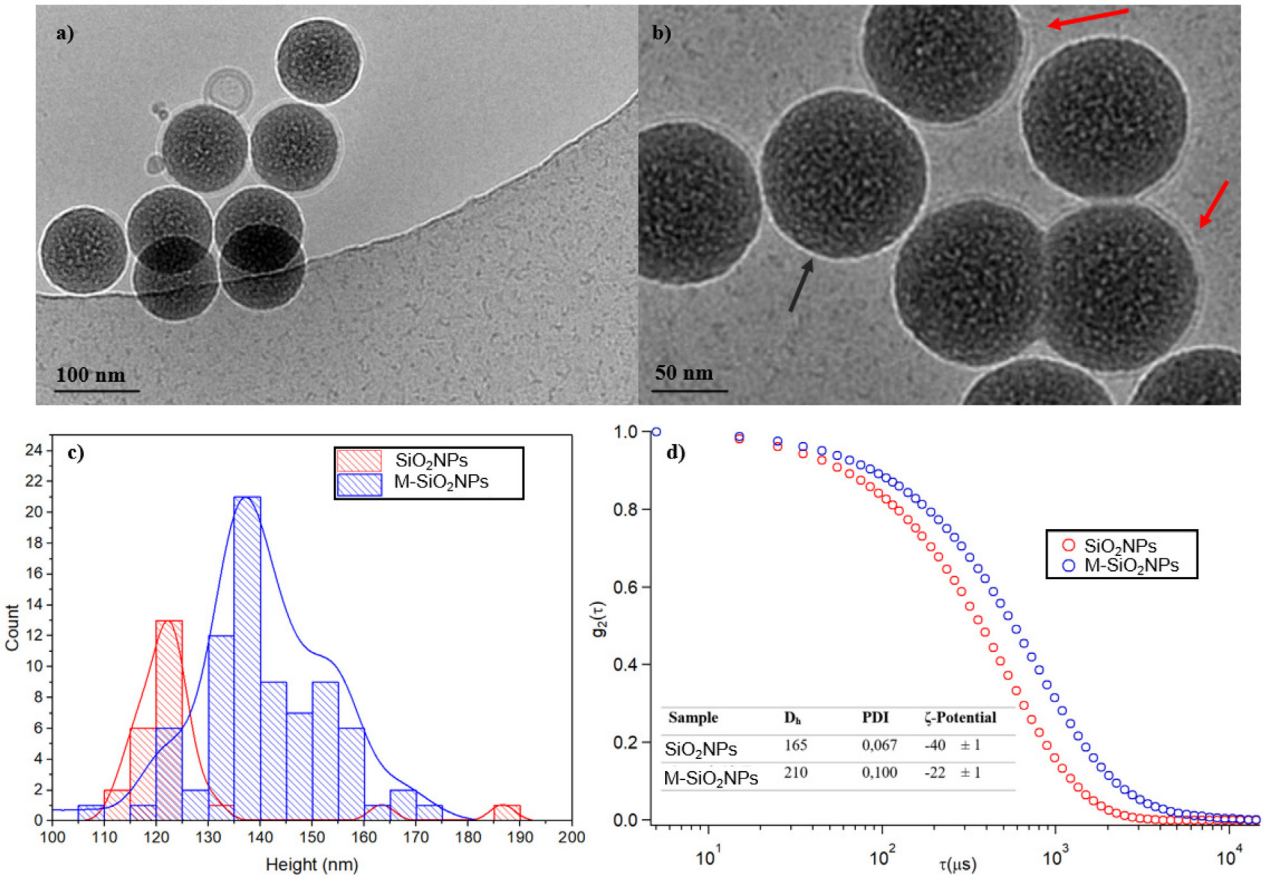

Fig. 1. a) and b) Cryo-EM images of M-M-SiO_2NPs at different magnifications (red and black arrows identify coated and uncoated areas of M-SiO_2NPs, respectively); c) Size distribution of SiO_2NPs (red) and M-SiO_2NPs (blue) obtained by liquid-AFM imaging; d) Autocorrelation functions of 0.08 mg/mL water dispersion of SiO_2NPs (red) and M-SiO_2NPs (blue). The inset shows the hydrodynamic diameter (extrapolated by a cumulant fitting) and the ζ -potential values of each sample. (For interpretation of the references to color in this figure legend, the reader is referred to the web version of this article.)

3.2. The interaction of M-SiO_2NPs with citrate-coated gold nanoparticles

Once the formation of M-M-SiO_2NPs was demonstrated via different complementary techniques, as discussed in the previous paragraph, we tested the possibility of probing the lipid layer covering the NPs utilizing the plasmonic properties of AuNPs. To this purpose, 1.15 nM bare SiO_2NPs (control sample) were first challenged by 6.13 nM Turkevich-Frens AuNPs with an average diameter of 12 nm (PDI 0.095) and −35 ± 3 mV ζ -Potential (see section S3 of SI for AuNPs characterization), for a final SiO_2NPs/AuNPs number ratio of ∼ 1/30. The sample was imaged via Cryo-EM (Fig. 2a), showing that AuNPs do not interact with bare SiO_2NPs, which is expected for the electrostatic repulsion between the two inorganic surfaces, both having a highly negative ζ -Potential. Conversely, when AuNPs are incubated with M-M-SiO_2NPs under the same conditions, a completely different effect is visible: as shown in Fig. 2b (see also section S4.1 for additional images), AuNPs spontaneously cluster on M-SiO_2NPs, forming AuNPs-decorated M-SiO_2NPs composites. This phenomenon, which did not occur with the bare SiO_2NPs, is clearly induced by the presence of a lipid bilayer on the SiO_2 surface, which mediates the adhesion and clustering of AuNPs on M-M-SiO_2NPs. Cryo-TEM results were complemented by an ensemble-averaged characterization performed through DLS (see section S4.2 of SI), which provided the mean size and polydispersity of SiO_2NPs/AuNPs and M-M-SiO_2NPs/AuNPs mixed samples. This characterization showed no interaction between AuNPs and bare SiO_2NPs, testified by the presence of two distinct populations within the SiO_2NPs/AuNPs sample, whose sizes perfectly match the ones of free AuNPs (∼20 nm) and free SiO_2NPs (∼170 nm). In contrast, a single population of bigger size (∼230 nm) was detected for the M-M-SiO_2NPs/AuNPs sample, consistent with the formation of composites in which M-SiO_2NPs are decorated by a layer of AuNPs. Remarkably, the clustering of AuNPs on M-M-SiO_2NPs led to an evident color change of the AuNPs dispersion from red to purple/blue (see insets of Fig. 2c and 2d) within 10 min of incubation, which can be noticed by the naked eye and is connected to a variation of AuNPs' plasmonic properties. Conversely, bare SiO_2NPs do not induce significant color variations in the AuNPs' dispersion. The corresponding spectral variations were quantified by means of UV–Vis spectroscopy (results displayed in Fig. 2c and 2d). In line with visual observation, the interaction of AuNPs with bare SiO_2NPs does not significantly alter the plasmonic features of AuNPs, consisting of the characteristic plasmonic primary peak located at 520 nm (red trace). On the contrary, the interaction with M-M-SiO_2NPs causes a red-shift of the plasmon resonance peak of AuNPs and the occurrence of an additional red-shifted shoulder, a well-established signature of plasmon coupling [90,91], consistent with AuNPs aggregation. As already anticipated, a similar coupling of the plasmons of AuNPs has been observed for AuNPs interacting with natural or synthetic vesicles and has been found to be triggered by AuNPs adhesion to the lipid membrane [81,89], driven by Van der Waals interactions, and promoted by the bending ability of the membrane [89–91]. Such phenomenon has been also conveniently used for determining the concentration, purity, and

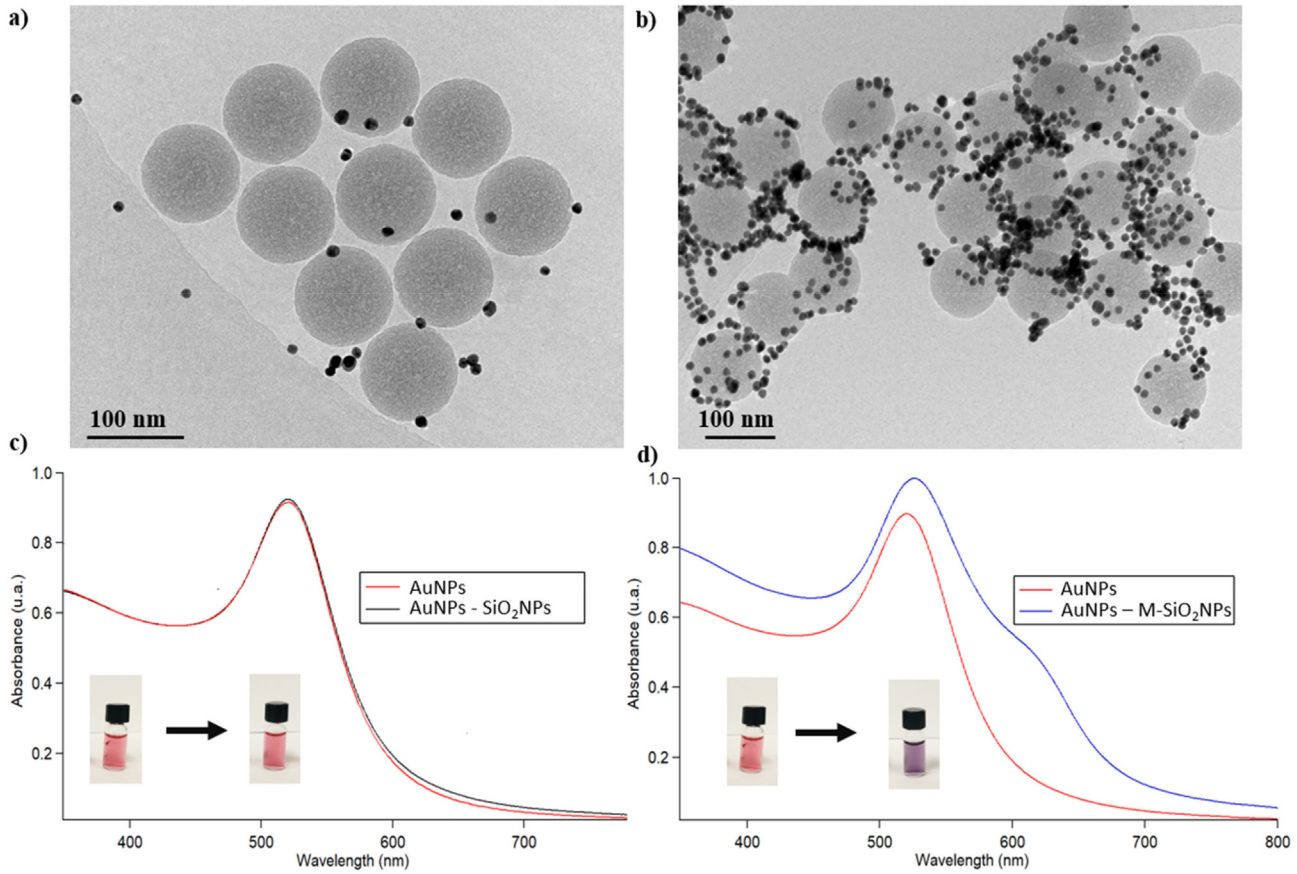

Fig. 2. Cryo-EM images of (a) SiO_2NPs/AuNPs, (b) M-SiO_2NPs/AuNPs composites, and UV − visible spectra of AuNPs incubated with (c) SiO_2NPs and (d) M-SiO_2NPs. The UV–Vis spectrum of bare AuNPs (red curve) is also reported as a control sample. The visual appearance of AuNPs before and after the incubation with SiO_2NPs and M-SiO_2NPs is reported in the insets of the graphs. See also Figure S11 of SI for UV–Vis control spectra of SiO_2NPs and M-SiO_2NPs in the absence of AuNPs. (For interpretation of the references to color in this figure legend, the reader is referred to the web version of this article.)

rigidity of such synthetic or natural vesicles [53,103]. Here for the first time, we show that this phenomenon can also be activated on rigid nanoparticles (such as inorganic SiO_2NPs), thanks to the mediating action of a lipid bilayer covering their surface. The clustering of AuNPs on free-standing bilayers was previously found to be promoted by the bending ability of the lipid membrane [87,89–91]; on the contrary, it was expected to be strongly suppressed (or fully prevented) for lipid interfaces formed on rigid supports (e.g., the inorganic core of NPs), where membrane bending ability is strongly reduced. To shed light on this aspect, we directly compared the UV–Vis spectra of AuNPs incubated with M-SiO_2NPs with the ones of AuNPs interacting with liposomes presenting the same membrane composition (see section S4.3 of SI); the results showed that the rigid core of SiO_2 strongly decreases the aggregation of AuNPs on the lipid membrane (likely due to the increment in the overall stiffness of M-SiO_2NPs composites with respect to pristine vesicles), without, however, completely preventing it. In fact, the clustering extent of AuNPs on M-M-SiO_2NPs is sufficient to detect an apparent color change in AuNPs dispersion and, accordingly, a variation in the corresponding UV–Vis absorbance spectra.

3.3. A nanoplasmonic assay to quantify lipid coverage in M-M-SiO_2NPs

Having demonstrated that the self-assembly of citrate-coated AuNPs occurs on lipid-coated SiO_2NPs and not on bare ones, we explored how the plasmonic variations of AuNPs are affected by the extent of lipid coverage of the SiO_2NPs. To this aim, we applied the same transmembrane osmotic shock-based protocol for synthesizing several SiO_2NPs samples with different degrees of coating (see Materials and Methods section). While a NP/vesicle ratio $\geq$1/50 is required to obtain almost full coverage of the silica surface (i.e., ∼88%, see previous paragraphs), the coverage extent can be tuned by varying the SiO_2NP/vesicle ratio during incubation. Employing SiO_2NPs/vesicles ratios of 1/50, 1/15, 1/10, 1/5, 1/3, and 1/1, we realized different hybrids and characterized them through ICP-AES, DLS, and ζ -potential (see Section 2.4). Table 1 provides a full overview of such characterization.

The results obtained from ICP-AES measurements were used for a rough estimation of the coating degrees of SiO_2NPs (see SI section S2.3). The coating fraction ranged from 13% to 88% by increasing the number of vesicles employed in the incubation step. The size, colloidal stability, and surface charge of the M-SiO_2NPs with different coating degrees were assessed by DLS and ζ -Potential. The ζ -Potential of the M-SiO_2NPs decreases in a monotonous trend, passing from −23 ± 1 mV for the 1/50 SiO_2NPs/vesicle ratio to −37 ± 4 mV for the 1/1 one, which is very close to the value obtained for bare SiO_2NPs. These results are consistent with an increased extent of particle coverage as the number of vesicles per SiO_2NP increases. On the other hand, the hydrodynamic size of M-SiO_2NPs is stable (around 200 nm) in the range 1/50 to 1/5 SiO_2NPs/vesicle ratio, while for higher ratios (i.e., 1/3 and 1/1) the samples display an abrupt increase in the size, reaching very high hydrodynamic diameters (400–600 nm) and polydispersity (around 0.3–0.4). For these dispersions, we observed low colloidal stability, with massive precipitation within 1 h from preparation. This observation can be explained considering that, for high SiO_2-NPs/vesicle ratios, the coverage on SiO_2NPs is only partial. In agreement with some recent reports, a lipid surface coverage lower than

Table 1
Hydrodynamic diameter, PDI and ζ -potential values of SiO_2NPs, bare vesicles, and M-SiO_2NPs obtained using different SiO_2NPs-vesicles ratios. The last column reports the SiO_2NPs coverage percentage, calculated from the concentration of P and Si measured by ICP-AES for each composition (see SI Section S2.3). The inset displays a schematic representation of how the coverage affects the size and stability of the hybrids.

Sample	D_h (nm)	PDI	Z-Potential (mV)	SiO_2NPs coverage
Vesicles	115	0.115	−11.2 ± 1.1	/
SiO_2NP	165	0.067	−40.2 ± 0.9	0%
1/50	210	0.100	−22.7 ± 1.3	88 ± 8%
1/15	193	0.122	−26.2 ± 1.2	68 ± 7%
1/10	189	0.164	−28.6 ± 0.7	60 ± 6%
1/5	193	0.152	−30.3 ± 1.4	53 ± 5%
1/3	414	0.363	−37.1 ± 3.2	33 ± 3%
1/1	621	0.335	−36.5 ± 3.5	13 ± 1%

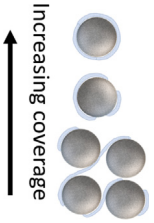

40% induces abrupt precipitation [104] due to the presence of membrane patches on the silica surface, triggering the bridging between different -and partially coated- particles [63,64] (inset in Table 1). In the present case, it is reasonable to assume that, for colloidally unstable samples, the vesicles' amount is too low to completely coat the available SiO_2 surface, and, therefore, most of the SiO_2NPs will present a discontinuous surface coverage. The lipid edges of the bilayer patches represent very high-energy spots, which promote interaction with other uncompleted bilayer shells, inducing particle bridging, and precipitation. In this hypothesis, the dispersions' stability, only achieved for lower SiO_2NPs/vesicle ratios (<1/3), can be considered an indirect proof of the formation of intact bilayer shells around the surface of a significant fraction of the SiO_2NPs.

We then investigated the interaction of AuNPs with M-SiO_2NPs presenting different coating degrees through UV–vis spectroscopy (Fig. 3a). For this purpose, the M-SiO_2NPs were incubated with AuNPs under the same experimental conditions described in section 2.2. The incubation provokes a gradual color variation of the original AuNPs dispersion (see Fig. 3a inset), from a ruby red to dif-

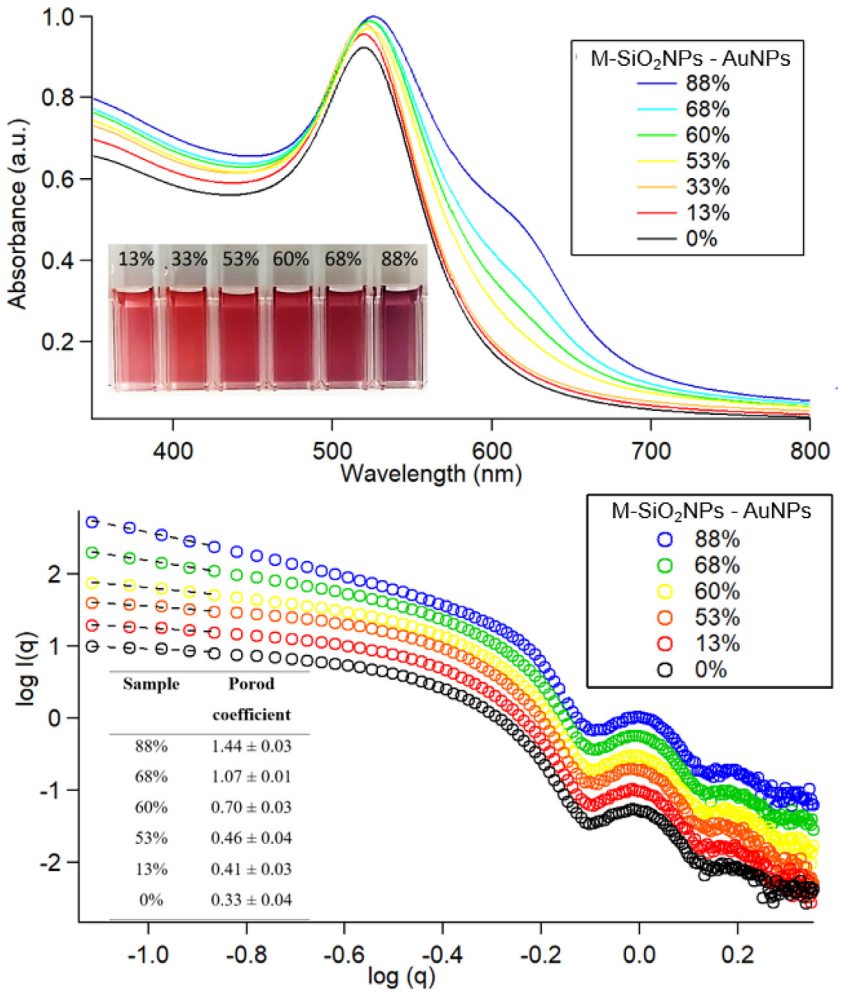

Fig. 3. (Top) UV − visible spectra of 6.13 nM AuNPs interacting with 1.15 nM M-SiO_2NPs with different degrees of coverage, collected after 10 min of incubation; (bottom) SAXS profiles of M-SiO_2NPs -AuNPs mixtures with varying degrees of SiO_2NPs membrane coverage collected after 10 min of incubation. The inset displays the Porod coefficients extracted from the linear fits (dashed black lines) of the double log plots.

ferent shades of purple; this is associated with a broadening of the plasmonic primary signal and the appearance of a red-shifted shoulder, previously also observed for the 1/50 SiO_2NPs/vesicles sample (section 2.2). Interestingly, the extent of such variations (especially in terms of the intensity of the red-shifted shoulder) depends on the fraction of membrane-covered SiO_2NPs surface. Specifically, the red-shifted shoulder gets gradually more pronounced with increasing membrane coverage.

To characterize the structure of the AuNP aggregates, we performed Synchrotron Small Angle X-Ray Scattering (SAXS) measurements (Elettra, Trieste, Italy). Fig. 3b displays the SAXS profiles obtained for the bare AuNPs and M-M-SiO_2NPs/AuNPs adducts. The scattering signal arises from a form factor P(q), which accounts for the shape and size of the dispersed objects, and from a structure factor S(q), which depends on interparticle interactions. In our experimental conditions, considering the much higher concentration of the AuNPs, the SiO_2NPs contribution to the scattering profiles can be regarded as negligible (see Fig. S12 in section S4.4). Therefore, the SAXS profiles shown in Fig. 3b are only due to the combination of the P(q) and the S(q) of AuNPs, providing specific information on their structure and aggregation extent. In particular, in the low-q range ($0.082 < nM\text{-}M^{-1} < 0.161$), we notice a power-law dependence between the scattering intensity and q, highlighted by a linear trend in a double-log representation of the profiles. For low scattering vectors values, the scattering signal accounts for the morphology of particles and aggregates. According to the Porod approximation [105], this dependence can be related to the mass fractal dimension of the probed objects, which accounts for the dimensionality of the AuNPs clusters. Specifically, the absolute values of the slopes of the log–log plots can be associated with a Porod coefficient which represents the fractal dimension of the aggregates. The evaluated slope decreases from −0.53 to −1.44 as the membrane coverage increases, as reported in the inset of Fig. 3b. In a model-free fashion, such a slope evolution suggests that the aggregation of AuNPs creates larger and more densely packed clusters with increasing SiO_2NPs coverage. Overall, the structural information gained from the SAXS profiles strongly agrees with the plasmonic variations monitored in the UV–Vis spectra.

The results from SAXS and UV–Vis show that AuNPs clustering on M-SiO_2NPs is spontaneous and strictly modulated by the coated surface fraction of SiO_2NPs. The plasmonic properties of AuNPs conveniently monitor such dependence through both color and spectral variations of the AuNPs/M-SiO_2NPs dispersion. It is then possible to infer the coating degree from a colorimetric assay by introducing a quantitative descriptor of the plasmonic variations of the AuNPs dispersion. To this aim, we selected an optical index recently used to quantify the variation of optical properties of AuNPs dispersions in the presence of synthetic free-standing vesicles [91]. This aggregation index (A.I.) is calculated by dividing the area subtended by the absorbance spectrum in the 560–800 nm range by the total spectral range area (350–800 nm). The results are then normalized for the A.I. of neat AuNPs, so that the A.I. of neat AuNPs' dispersion is equal to 1 and, increasing the particle aggregation, the A.I. value increases. Table 2 summarizes the A.I.s for each M-SiO_2NPs/AuNPs sample, where the coating degrees vary.

Fig. 4 shows the so-determined A.I. values plotted *versus* the membrane coverage % of SiO_2NPs (inferred quantitatively by ICP-AES). While the gradual color variation of AuNPs (bottom inset in Fig. 4) can already provide some qualitative hints on the degree of membrane coverage, the A.I. and the coverage extent of SiO_2NPs are linked by a precise functional relation, which paves the way for developing a spectrophotometric assay for the quantitative determination of membrane coverage. Specifically, the A.I. increases linearly with membrane coverage (r-squared 0.98) over a wide range of coating yields (35–90%). The fitting accuracy decreases when

Table 2
A.I. values obtained for each different membrane coverage of SiO_2NPs.

SiO_2NPs coverage	A.I.
88%	1.81 ± 0.05
68%	1.63 ± 0.04
60%	1.45 ± 0.03
53%	1.35 ± 0.02
33%	1.14 ± 0.01
13%	1.07 ± 0.02
0%	1

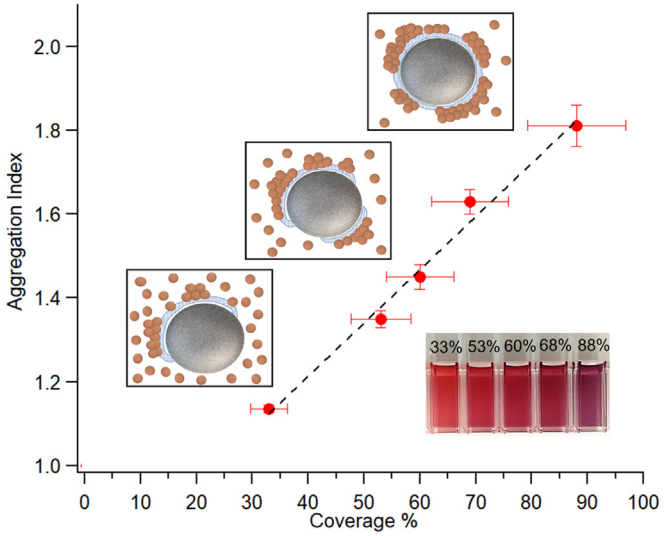

Fig. 4. A.I. as a function of SiO_2NPs membrane coverage, with sketches of AuNPs/M-M-SiO_2 hybrids highlighting how the integrity of the membrane coating affects AuNPs binding and aggregation. Inset: visual appearance of AuNPs incubated with SiO_2NPs at different membrane coverages.

SiO_2NPs with a coverage <35% are included in the linear regression, yielding an r-squared of 0.95 (see section 5.2 of SI). This is probably due to the poor colloidal stability of the M-M-SiO2NPs in low coverage conditions, leading to uncontrolled precipitation of M-SiO_2NPs/AuNPs complexes (see Fig. S14 of SI for the correlation between the hydrodynamic size of M-SiO_2NPs and the optical response of AuNPs).

While several qualitative methods (e.g., colloidal stability tests [67], and sodium dodecyl sulfate–polyacrylamide gel electrophoresis [74]) can easily detect a very poor (<35%) or absent coverage on NPs, this approach offers a precise -and quantitative- determination of membrane integrity at intermediate and/or high membrane coverage levels, which represents the compositional range of interest for the application of NPs in the biomedical field; as a matter of fact, most of the membrane-related surface functionalities of NPs vanish at low coverages [68–70], while only higher levels of coverage ensure colloidal stability [62,64] of NPs and partial (or complete) preservation of the biological functions [67] of their membrane shell.

Moreover, it is worth noticing that since the aggregation of AuNPs is induced by the presence of the lipid bilayer coating, the assay does not depend on the chemical nature of the nanoparticles' inorganic core and could be extended to NPs with different compositions and physicochemical features.

4. Conclusions

In the last years, the production of lipid bilayer-coated materials has proved a powerful approach to increase the biocompatibil-

ity of inorganic NPs, reduce adverse side effects, and improve their efficiency. To reach this overarching goal, high-fidelity structural control and the availability of analytical methods amenable to scale-up production are critical. Here we described a straightforward and quantitative assay for determining the extent of biomimetic lipid bilayer coverage on inorganic nanoparticles. Based on previous works, we leveraged the plasmonic properties of Turkevich-Frens AuNPs and their sensitivity to the AuNP aggregation extent to develop an effective method for the quantification of lipid membrane coating on inorganic NPs. By challenging SiO_2NPs of different -and known- lipid coverage degrees with AuNPs, we show that, in the region of colloidal stability, the plasmonic descriptor of AuNPs' optical properties linearly varies with the amount of lipid coverage and that this dependence can be leveraged for estimating the coverage extent. As a difference from the already available methods [71–73,78–80], such assay provides a fast and high-throughput readout of membrane integrity at an ensemble-averaged level, which only requires cheap reagents, standard lab instrumentation, and limited users experience. From a different -but equally important- perspective, we also showed that a lipid membrane could drive and control the self-assembly of AuNPs on an inorganic nanosized scaffold, which enables the possibility of creating complex hybrid materials composed of an inorganic core, a lipid bilayer shell and a further plasmonic shell of tuneable optical properties. The easiness of preparation, which exploits the spontaneous self-assembly of AuNPs, can inspire the production of multicomponent biocompatible nanomaterials with high structural fidelity and mild experimental conditions.

Funding Sources.

This work has been supported by the European Community through the BOW project (H2020-EIC-FETPROACT2019, ID 952183). We also acknowledge MIUR-Italy (“Progetto Dipartimenti di Eccellenza 2018–2022, ref B96C1700020008” allocated to the Department of Chemistry “Ugo Schiff”) and Ente Cassa di Risparmio di Firenze for economic support.

CRediT authorship contribution statement

Jacopo Cardellini: Investigation, Methodology, Formal analysis, Writing – original draft. **Andrea Ridolfi:** Investigation, Formal analysis, Writing – review & editing. **Melissa Donati:** Investigation. **Valentina Giampietro:** Investigation. **Mirko Severi:** Investigation. **Marco Brucale:** Investigation, Writing – review & editing. **Francesco Valle:** Investigation, Writing – review & editing. **Paolo Bergese:** Funding acquisition, Writing – review & editing. **Costanza Montis:** Investigation, Writing – review & editing. **Lucrezia Caselli:** Conceptualization, Investigation, Methodology, Formal analysis, Supervision, Writing – original draft, Writing – review & editing. **Debora Berti:** Conceptualization, Methodology, Supervision, Project administration, Funding acquisition, Writing – review & editing.

Data availability

Data will be made available on request.

Declaration of Competing Interest

The authors declare that they have no known competing financial interests or personal relationships that could have appeared to influence the work reported in this paper.

Acknowledgements

Prof. Paolo Arosio and Karl Normak (Biochemical Engineering Laboratory, ETH Zurich, Switzerland) are acknowledged for sharing their knowledge on the membrane composition and preparation of the liposomal models for EVs employed herein, as well as for fruitful discussion on the design of M-SiO_2NPs. The Elettra Synchrotron SAXS facility (Basovizza, Trieste, Italy) is acknowledged for beam time (Proposal id: 20212182). We acknowledge the Florence Center for Electron Nanoscopy (FloCEN) at the University of Florence.

Appendix A. Supplementary material

Supplementary data to this article can be found online at https://doi.org/10.1016/j.jcis.2023.02.073.

References

[1] S. Gavas, S. Quazi, T.M. Karpiński, Nanoscale Res. Lett. 16 (2021) 173.
[2] S. Hua, M.B.C. de Matos, J.M. Metselaar, G. Storm, Front. Pharmacol. 10.3389/fphar.2018.00790.
[3] M. Henriksen-Lacey, S. Carregal-Romero, L.M. Liz-Marzán, Bioconjug. Chem. 28 (2017) 212–221.
[4] M. Hofmann-Amtenbrink, D.W. Grainger, H. Hofmann, Nanomedicine Nanotechnology, Biol. Med. 11 (2015) 1689–1694.
[5] S. Barua, S. Mitragotri, Nano Today 9 (2014) 223–243.
[6] E. Pedziwiatr-Werbicka, K. Horodecka, D. Shcharbin, M. Bryszewska, Curr. Med. Chem. 28 (2020) 346–359.
[7] N. Zhang, J. Lin, S.Y. Chew, A.C.S. Appl, Mater. Interfaces 13 (2021) 55840–55850.
[8] X. Zhen, P. Cheng, K. Pu, Small 15 (2019) 1–19.
[9] M. Wu, W. Le, T. Mei, Y. Wang, B. Chen, Z. Liu, C. Xue, Int. J. Nanomed. 14 (2019) 4431–4448.
[10] R.H. Fang, C.M.J. Hu, B.T. Luk, W. Gao, J.A. Copp, Y. Tai, D.E. O'Connor, L. Zhang, Nano Lett. 14 (2014) 2181–2188.
[11] L. Zhang, X. Zhang, G. Lu, F. Li, W. Bao, C. Song, W. Wei, G. Ma, Small 15 (2019) 1–13.
[12] M. Zhou, Y. Xing, X. Li, X. Du, T. Xu, X. Zhang, Small 16 (2020) 1–11.
[13] M.M. Van Schooneveld, E. Vucic, R. Koole, Y. Zhou, J. Stocks, D.P. Cormode, C.Y. Tang, R.E. Gordon, K. Nicolay, A. Meijerink, Z.A. Fayad, W.J.M. Mulder, Nano Lett. 8 (2008) 2517–2525.
[14] A. Luchini, G. Vitiello, Front. Chem. 7 (2019) 1–16.
[15] J. Yang, J. Tu, G.E.M. Lamers, R.C.L. Olsthoorn, A. Kros, Adv. Healthc. Mater. 6 (2017) 1–7.
[16] K.S. Butler, P.N. Durfee, C. Theron, C.E. Ashley, E.C. Carnes, C.J. Brinker, Small 12 (2016) 2173–2185.
[17] G.D. Bothun, J. Nanobiotechnol. 6 (2008) 1–10.
[18] M. Sancho-Albero, M. del M. Encabo-Berzosa, M. Beltrán-Visiedo, L. Fernández-Messina, V. Sebastián, F. Sánchez-Madrid, M. Arruebo, J. Santamaría and P. Martín-Duque, Nanoscale **11** (2019) 18825–18836.
[19] M. Sancho-Albero, B. Rubio-Ruiz, A.M. Pérez-López, V. Sebastián, P. Martín-Duque, M. Arruebo, J. Santamaría, A. Unciti-Broceta, Nat. Catal. 2 (2019) 864–872.
[20] C.-M.-J. Hu, L. Zhang, S. Aryal, C. Cheung, R.H. Fang, L. Zhang, Proc. Natl. Acad. Sci. 108 (2011) 10980–10985.
[21] C. Ferrel, S. Rayamajhi, T. Nguyen, R. Marasini, T. Saravanan, F. Deba, S. Aryal, A.C.S. Appl, Bio Mater. 4 (2021) 6974–6981.
[22] J. Peng, Q. Yang, W. Li, L. Tan, Y. Xiao, L. Chen, Y. Hao, Z. Qian, A.C.S. Appl, Mater. Interfaces 9 (2017) 44410–44422.
[23] Q. Pei, X. Hu, X. Zheng, S. Liu, Y. Li, X. Jing, Z. Xie, ACS Nano 12 (2018) 1630–1641.
[24] J.P. Thawani, A. Amirshaghaghi, L. Yan, J.M. Stein, J. Liu, A. Tsourkas, Small 13 (2017) 1–9.
[25] S. Krishnamurthy, M.K. Gnanasammandhan, C. Xie, K. Huang, M.Y. Cui, J.M. Chan, Nanoscale 8 (2016) 6981–6985.
[26] H. Zhao, L. Li, J. Zhang, C. Zheng, K. Ding, H. Xiao, L. Wang, Z. Zhang, A.C.S. Appl, Mater. Interfaces 10 (2018) 31124–31135.
[27] L. Rao, Z. He, Q.-F. Meng, Z. Zhou, L.-L. Bu, S.-S. Guo, W. Liu, X.-Z. Zhao, J. Biomed. Mater. Res. Part A 105 (2017) 521–530.
[28] Z. Chen, P. Zhao, Z. Luo, M. Zheng, H. Tian, P. Gong, G. Gao, H. Pan, L. Liu, A. Ma, H. Cui, Y. Ma, L. Cai, ACS Nano 10 (2016) 10049–10057.
[29] C. Liu, D. Wang, S. Zhang, Y. Cheng, F. Yang, Y. Xing, T. Xu, H. Dong, X. Zhang, ACS Nano 13 (2019) 4267–4277.
[30] J.-Y. Zhu, D.-W. Zheng, M.-K. Zhang, W.-Y. Yu, W.-X. Qiu, J.-J. Hu, J. Feng, X.-Z. Zhang, Nano Lett. 16 (2016) 5895–5901.
[31] Z. Gao, L. Zhang, J. Hu, Y. Sun, Nanomedicine nanotechnology, Biol. Med. 9 (2013) 174–184.
[32] X. Geng, D. Gao, D. Hu, Q. Liu, C. Liu, Z. Yuan, X. Zhang, X. Liu, Z. Sheng, X. Wang, H. Zheng, A.C.S. Appl, Mater. Interfaces 12 (2020) 55624–55637.

[33] Q. Jiang, K. Wang, X. Zhang, B. Ouyang, H. Liu, Z. Pang, W. Yang, Small 16 (2020) 2001704.
[34] C.-H. Luo, C.-T. Huang, C.-H. Su, C.-S. Yeh, Nano Lett. 16 (2016) 3493–3499.
[35] D.T. Riglar, P.A. Silver, Nat. Rev. Microbiol. 16 (2018) 214–225.
[36] V. Gujrati, S. Kim, S.-H. Kim, J.J. Min, H.E. Choy, S.C. Kim, S. Jon, ACS Nano 8 (2014) 1525–1537.
[37] T. Kang, Q. Zhu, D. Wei, J. Feng, J. Yao, T. Jiang, Q. Song, X. Wei, H. Chen, X. Gao, J. Chen, ACS Nano 11 (2017) 1397–1411.
[38] Y. Fu, G. He, Z. Liu, J. Wang, M. Li, Z. Zhang, Q. Bao, J. Wen, X. Zhu, C. Zhang, W. Zhang 2202337 (2022) 1–11
[39] M. Wu, X. Liu, H. Bai, L. Lai, Q. Chen, G. Huang, B. Liu, G. Tang, A.C.S. Appl, Mater. Interfaces 11 (2019) 9850–9859.
[40] J. Li, X. Zhen, Y. Lyu, Y. Jiang, J. Huang, K. Pu, ACS Nano 12 (2018) 8520–8530.
[41] L. Rao, B. Cai, L.-L. Bu, Q.-Q. Liao, S.-S. Guo, X.-Z. Zhao, W.-F. Dong, W. Liu, ACS Nano 11 (2017) 3496–3505.
[42] X. Zhen, P. Cheng, K. Pu, Small 15 (2019) 1804105.
[43] L. Zhu, Y. Zhong, S. Wu, M. Yan, Y. Cao, N. Mou, G. Wang, D. Sun, W. Wu, Mater. Today Bio 14 (2022) 100228.
[44] D. Wang, C. Liu, S. You, K. Zhang, M. Li, Y. Cao, C. Wang, H. Dong, X. Zhang, A.C. S. Appl, Mater. Interfaces 12 (2020) 41138–41147.
[45] J.R. Fitzgerald, T.J. Foster, D. Cox, Nat. Rev. Microbiol. 4 (2006) 445–457.
[46] C.-M.-J. Hu, R.H. Fang, J. Copp, B.T. Luk, L. Zhang, Nat. Nanotechnol. 8 (2013) 336–340.
[47] Q. Zhang, D. Dehaini, Y. Zhang, J. Zhou, X. Chen, L. Zhang, R.H. Fang, W. Gao, L. Zhang, Nat. Nanotechnol. 13 (2018) 1182–1190.
[48] H.-W. Chen, Z.-S. Fang, Y.-T. Chen, Y.-I. Chen, B.-Y. Yao, J.-Y. Cheng, C.-Y. Chien, Y.-C. Chang, C.-M.-J. Hu, A.C.S. Appl, Mater. Interfaces 9 (2017) 39953–39961.
[49] P. Fathi, L. Rao, X. Chen, View 2 (2021) 20200187.
[50] R. Van Der Meel, M.H.A.M. Fens, P. Vader, W.W. Van Solinge, O. Eniola-Adefeso, R.M. Schiffelers, J. Control. Release 195 (2014) 72–85.
[51] G. Raposo, W. Stoorvogel, J. Cell Biol. 200 (2013) 373–383.
[52] H. Saari, E. Lázaro-Ibáñez, T. Viitala, E. Vuorimaa-Laukkanen, P. Siljander, M. Yliperttula, J. Control. Release 220 (2015) 727–737.
[53] S. Busatto, A. Giacomini, C. Montis, R. Ronca, P. Bergese, Anal. Chem. 90 (2018) 7855–7861.
[54] S. Kamerkar, V.S. LeBleu, H. Sugimoto, S. Yang, C.F. Ruivo, S.A. Melo, J.J. Lee, R. Kalluri, Nature 546 (2017) 498–503.
[56] S. el Andaloussi, S. Lakhal, I. Mäger, M.J.A. Wood, Adv. Drug Deliv. Rev. 65 (2013) 391–397.
[57] M.J. Haney, N.L. Klyachko, Y. Zhao, R. Gupta, E.G. Plotnikova, Z. He, T. Patel, A. Piroyan, M. Sokolsky, A.V. Kabanov, E.V. Batrakova, J. Control. Release 207 (2015) 18–30.
[58] O.M. Elsharkasy, J.Z. Nordin, D.W. Hagey, O.G. de Jong, R.M. Schiffelers, S. EL Andaloussi, P. Vader, Adv. Drug Deliv. Rev. 159 (2020) 332–343.
[59] C. Liu, W. Zhang, Y. Li, J. Chang, F. Tian, F. Zhao, Y. Ma, J. Sun, Nano Lett. 19 (2019) 7836–7844.
[60] G. Cheng, W. Li, L. Ha, X. Han, S. Hao, Y. Wan, Z. Wang, F. Dong, X. Zou, Y. Mao, S.-Y. Zheng, J. Am. Chem. Soc. 140 (2018) 7282–7291.
[61] J. Wang, Y. Dong, Y. Li, W. Li, K. Cheng, Y. Qian, G. Xu, X. Zhang, L. Hu, P. Chen, W. Du, X. Feng, Y. Di Zhao, Z. Zhang, B.F. Liu, Adv. Funct. Mater. 28 (2018) 1–14.
[62] A.H. Bahrami, M. Raatz, J. Agudo-canalejo, R. Michel, E.M. Curtis, C.K. Hall, M. Gradzielski, R. Lipowsky, T.R. Weikl, M. Raphael, C.E.M,H.C.K,G. Michael, L. Rein, Adv. Colloid Interface Sci. 10.1016/j.cis.2014.02.012.
[63] R. Michel, M. Gradzielski, Int. J. Mol. Sci. 13 (2012) 11610–11642.
[64] S. Mornet, O. Lambert, E. Duguet, A. Brisson, Nano Lett. 5 (2005) 281–285.
[65] J. Liu, X. Jiang, C. Ashley, C.J. Brinker, J. Am. Chem. Soc. 131 (2009) 7567–7569.
[66] J. Van Deun, Q. Roux, S. Deville, T. Van Acker, P. Rappu, I. Miinalainen, J. Heino, F. Vanhaecke, B.G. De Geest, O. De Wever, A. Hendrix, Cells 9 (2020) 1797.
[67] L. Liu, X. Bai, M.-V. Martikainen, A. Kårlund, M. Roponen, W. Xu, G. Hu, E. Tasciotti, V.-P. Lehto, Nat. Commun. 12 (2021) 5726.
[68] M. Hadjidemetriou, Z. Al-Ahmady, M. Mazza, R.F. Collins, K. Dawson, K. Kostarelos, ACS Nano 9 (2015) 8142–8156.
[69] F. Persson, J. Fritzsche, K.U. Mir, M. Modesti, F. Westerlund, J.O. Tegenfeldt, Nano Lett. 12 (2012) 2260–2265.
[70] R.C. Van Lehn, M. Ricci, P.H.J. Silva, P. Andreozzi, J. Reguera, K. Voïtchovsky, F. Stellacci, A. Alexander-Katz, Nat. Commun. 5 (2014) 4482.
[71] A.E. LaBauve, T.E. Rinker, A. Noureddine, R.E. Serda, J.Y. Howe, M.B. Sherman, A. Rasley, C.J. Brinker, D.Y. Sasaki, O.A. Negrete, Sci. Rep. 8 (2018) 13990.
[72] D.B. Tada, E. Suraniti, L.M. Rossi, C.A.P. Leite, C.S. Oliveira, T.C. Tumolo, R. Calemczuk, T. Livache, M.S. Baptista, J. Biomed. Nanotechnol. 10 (2014) 519–528.
[73] C. Gao, Q. Huang, C. Liu, C.H.T. Kwong, L. Yue, J.-B. Wan, S.M.Y. Lee, R. Wang, Nat. Commun. 11 (2020) 2622.
[74] W. Liu, M. Zou, T. Liu, J. Zeng, X. Li, W. Yu, C. Li, J. Ye, W. Song, J. Feng, X. Zhang, Nat. Commun., 1–12.
[75] L. Zhang, Y. Zhu, X. Wei, X. Chen, Y. Li, Y. Zhu, J. Xia, Y. Huang, Y. Huang, J. Wang, Z. Pang, Acta Pharm. Sin. B 12 (2022) 3427–3447.
[76] J. Zhuang, H. Gong, J. Zhou, Q. Zhang and W. Gao.
[77] W. Liu, M. Zou, T. Liu, J. Zeng, X. Li, W. Yu, C. Li 1900499 (2019) 1–10.
[78] L.P. Arnett, M.W. Forbes, R. Keunen, M.A. Winnik, Langmuir 37 (2021) 14605–14613.
[79] J.Y. Lee, H. Wang, G. Pyrgiotakis, G.M. DeLoid, Z. Zhang, J. Beltran-Huarac, P. Demokritou, W. Zhong, Anal. Bioanal. Chem. 410 (2018) 6155–6164.
[80] X. Zhang, A. K. Pandiakumar, R. J. Hamers and C. J. Murphy, 10.1021/acs.analchem.8b03911.
[81] R. Kariuki, R. Penman, S.J. Bryant, R. Orrell-Trigg, N. Meftahi, R.J. Crawford, C.F. McConville, G. Bryant, K. Voïtchovsky, C.E. Conn, A.J. Christofferson, A. Elbourne, ACS Nano 16 (2022) 17179–17196.
[82] K. Sugikawa, T. Kadota, K. Yasuhara, A. Ikeda, Angew. Chemie - Int. Ed. 55 (2016) 4059–4063.
[83] F. Wang, J. Liu, Nanoscale 7 (2015) 15599–15604.
[84] F. Wang, D.E. Curry, J. Liu, Langmuir 31 (2015) 13271–13274.
[85] C. Montis, D. Maiolo, I. Alessandri, P. Bergese, D. Berti, Nanoscale 6 (2014) 6452–6457.
[86] S. Salassi, L. Caselli, J. Cardellini, E. Lavagna, C. Montis, D. Berti, G. Rossi, J. Chem. Theory Comput. 17 (2021) 6597–6609.
[87] J. Cardellini, C. Montis, F. Barbero, I. De Santis, L. Caselli, D. Berti, Front. Bioeng. Biotechnol., 10.3389/fbioe.2022.848687.
[88] A. Ridolfi, L. Caselli, C. Montis, G. Mangiapia, D. Berti, M. Brucale, F. Valle, J. Microsc. 280 (2020) 194–203.
[89] C. Montis, L. Caselli, F. Valle, A. Zendrini, F. Carlà, R. Schweins, M. Maccarini, P. Bergese, D. Berti, J. Colloid Interface Sci. 573 (2020) 204–214.
[90] J. Cardellini, L. Caselli, E. Lavagna, S. Salassi, H. Amenitsch, M. Calamai, C. Montis, G. Rossi, D. Berti, J. Phys. Chem. C 126 (2022) 4483–4494.
[91] L. Caselli, A. Ridolfi, J. Cardellini, L. Sharpnack, L. Paolini, M. Brucale, F. Valle, C. Montis, P. Bergese, D. Berti, Nanoscale Horizons 6 (2021) 543–550.
[92] D. Maiolo, L. Paolini, G. Di Noto, A. Zendrini, D. Berti, P. Bergese, D. Ricotta, Anal. Chem. 87 (2015) 4168–4176.
[93] J. Turkevich, P.C. Stevenson, J. Hillier, Discuss. Faraday Soc. 11 (1951) 55–75.
[94] G. Frens, Nat. Phys. Sci. 241 (1973) 20–22.
[95] J.L. Hutter, J. Bechhoefer, Rev. Sci. Instrum. 64 (1993) 1868–1873.
[96] D.J. Müller, D. Fotiadis, S. Scheuring, S.A. Müller, A. Engel, Biophys. J. 76 (1999) 1101–1111.
[97] J.G. Croissant, K.S. Butler, J.I. Zink, C.J. Brinker, Nat. Rev. Mater. 5 (2020) 886–909.
[98] A. Watermann, J. Brieger, Nanomaterials, 10.3390/nano7070189.
[99] A. Llorente, T. Skotland, T. Sylvänne, D. Kauhanen, T. Róg, A. Orłowski, I. Vattulainen, K. Ekroos, K. Sandvig, Biochim. Biophys. Acta - Mol. Cell Biol Lipids 1831 (2013) 1302–1309.
[100] P.J. Chung, H.L. Hwang, K. Dasbiswas, A. Leong, K.Y.C. Lee, Langmuir 34 (2018) 13000–13005.
[101] P.A. Hassan, S. Rana, G. Verma, Langmuir 31 (2015) 3–12.
[102] M. Kaasalainen, V. Aseyev, E. von Haartman, D.Ş. Karaman, E. Mäkilä, H. Tenhu, J. Rosenholm, J. Salonen, Nanoscale Res. Lett. 12 (2017) 74.
[103] A. Zendrini, L. Paolini, S. Busatto, A. Radeghieri, M. Romano, M.H.M. Wauben, M.J.C. van Herwijnen, P. Nejsum, A. Borup, A. Ridolfi, C. Montis, P. Bergese, Front. Bioeng. Biotechnol. 7 (2020) 1–10.
[104] S. Savarala, F. Monson, M.A. Ilies, S.L. Wunder, Langmuir 27 (2011) 5850–5861.
[105] L.A. Feigin, D.I. Svergun, Structure Analysis by Small-Angle X-Ray and Neutron Scattering, Springer, US, Boston, MA, 1987.